REPORT DOCUMENTATION PAGE

Form Approved
OMB NO. 0704-0188

1. AGENCY USE ONLY (Leave Blank)	2. REPORT DATE -	3. REPORT TYPE AND DATES COVERED FINAL 01 Sep 00 - 28 Feb 01

4. TITLE AND SUBTITLE

Technology Options for Multi-specttral Infrared Cameras

5. FUNDING NUMBERS

DAAD19-00-1-0498

6. AUTHOR(S)

Griff Bilbro

7. PERFORMING ORGANIZATION NAME(S) AND ADDRESS(ES)

North Carolina State University

8. PERFORMING ORGANIZATION REPORT NUMBER

9. SPONSORING / MONITORING AGENCY NAME(S) AND ADDRESS(ES)

U. S. Army Research Office
P.O. Box 12211
Research Triangle Park, NC 27709-2211

10. SPONSORING / MONITORING AGENCY REPORT NUMBER

41627.1-CI-II

11. SUPPLEMENTARY NOTES

The views, opinions and/or findings contained in this report are those of the author(s) and should not be construed as an official Department of the Army position, policy or decision, unless so designated by other documentation.

12 a. DISTRIBUTION / AVAILABILITY STATEMENT

Approved for public release; distribution unlimited.

12 b. DISTRIBUTION CODE

13. ABSTRACT (Maximum 200 words)

Investigates the adaptation of Bayer color arrays as used in commercial of the shelf cameras to separate red, blue, and green spectra to multispectral infrared image sensors. Technology for filters on each pixel element for a spectral band is investigated and the demosaicing where values of the spectral bounds not sampled at certain locations are estimated from their neighbors.

14. SUBJECT TERMS

15. NUMBER OF PAGES
37

16. PRICE CODE

17. SECURITY CLASSIFICATION OR REPORT	18. SECURITY CLASSIFICATION ON THIS PAGE	19. SECURITY CLASSIFICATION OF ABSTRACT	20. LIMITATION OF ABSTRACT
UNCLASSIFIED	UNCLASSIFIED	UNCLASSIFIED	UL

Technology Options for Multi-Spectral Infrared Cameras

Final Technical Report for

Research Agreement No. DAAD19-00-01-0498

October 23, 2001

submitted to Dr. William Sander

Associate Director,

Computing & Information Science Division

US Army Research Office

by Dr. Griff L. Bilbro

Professor of Electrical and Computer Engineering

North Carolina State University

Raleigh, NC 27695-7911

Abstract

This report comprises the concluding analysis entitled "Robust Multispectral Imaging Sensors for Autonomous Robots" of the project as well as three additional documents. First, a complete report comparing alternative demosaicking algorithms for early processing of the sensors we are proposing. Second, a revision of a PowerPoint presentation of the final report for this project. provided in 3/01 for ARO. Third, the title page of Mr. Rajeev Ramanath's Master's Thesis, which was accepted in 8/01 by NCSU.

Robust Multispectral Imaging Sensors for Autonomous Robots

Rajeev Ramanath, *Student Member, IEEE*
Wesley E. Snyder, *Senior Member, IEEE*
Griff L. Bilbro, *Senior Member, IEEE*
William A. Sander

***Abstract*—Use of multispectral capability in imaging devices provide us with spectral characteristics of the objects being viewed. This helps in "recognizing" the object without any knowledge of the geometry or shape of the desired target. Until recently, multispectral images were obtained using multiple filters placed in front of the imaging devices or by using prism based beam-splitting technologies. With the advent of Digital Still Color Cameras, a whole new field of imaging has emerged, which consists of a monolithic array of color filters overlaid on a CCD array such that each pixel samples one spectral band. The resulting mosaic of spectral samples is processed to produce a high resolution color image where the values of the spectral bands not sampled at a certain location are estimated from its neighbors. This process is often referred to as *demosaicking*. This paper proposes the use of this technology as a general imaging modality for robust robot vision and compares several demosaicking algorithms.**

***Index Terms*—Multispectral, demosaicking, demosaicing, Color Filter Array, hexagonal sampling**

I. Introduction

OBTAINING multiple spectral samples of an object provide us with its spectral signature, which under many circumstances is of crucial importance. The plethora of information obtained from a color picture when compared to a grayscale picture, the wealth of information in obtaining a spectral signature of an enemy tank when compared to an integrated monochromatic image, the advantages of identifying vegetation, rocks, minerals, etc. from a satellite with multispectral capability, rather than single channel information cannot be overstated. In fig.1, we show the reflectivities of four different objects [1], the identification of which are critical for military purposes; especially for target seeking missiles or reconnaissance missions. Notice that the visible band would not be as useful as a combination of visible and MWIR bands which clearly provides unique spectral signatures for camouflaged military vehicles. Other applications for multispectral imagery have been found in glaciology, hydrology, volcanology, geological surveys[2], monitoring urban change[3] etc.

Department of Electrical and Computer Engineering
North Carolina State University, Raleigh, NC, 27695-7914, USA
Phone: (919) 513-2007, email: rramana@eos.ncsu.edu
Department of Electrical and Computer Engineering
North Carolina State University, Raleigh, NC, 27695-7914, USA
Phone: (919) 515-5114, email: wes@eos.ncsu.edu
Department of Electrical and Computer Engineering
North Carolina State University, Raleigh, NC, 27695-7911, USA
Phone: (919) 515-5101, email: glb@eos.ncsu.edu
U.S. Army Research Office
P.O. Box 12211, Research Triangle Park, NC 27709
Phone: (919) 529-4241, email: sander@arl.aro.army.mil

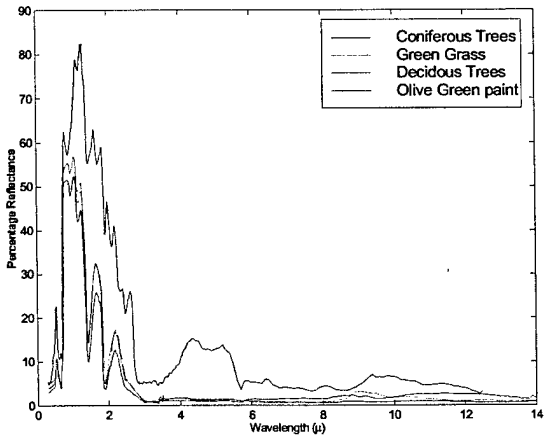

Fig. 1. Reflectivities of a few targets critical for detecting camouflage in battlefields

The classical approach to multispectral imaging is to use separate sensors and to somehow split the optical path to fall on those sensors in a manner which retains registration (or is later registered). For example in 3 CCD cameras, typically the light from the lens passes through a prism, is split into three rays, then through three different filters and onto three different focal plane detectors (see fig.2).

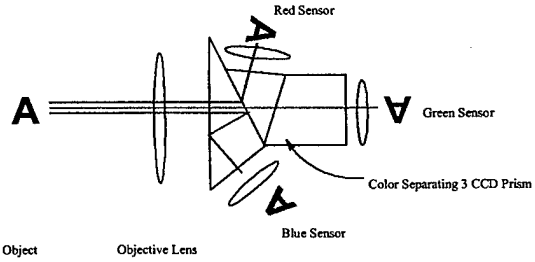

Fig. 2. 3 sensor configuration on most multispectral cameras

On satellite or airborne sensors, the optical path might be deflected by a moving mirror onto an array of sensors (*e.g.* MODIS/ASTER use "whiskbroom" scanning mirrors). Both approaches have the inherent problem of registration of the images. In addition, such sensors simply cannot tolerate the vibrations and accelerations of a mobile robot.

In [4] reconnaissance and surveillance robots are described, each provided with a suite of sensors. A mosaicked set of sensors as proposed here would be of immense use in such missions, providing multispectral capability along with ruggedness.

Airborne systems, robot platforms, missiles, etc. are used under "high stress" situations which require that the imaging system perform independent of the systems' vibration and acceleration. Multiple sensor systems are difficult

to manufacture with this capability. Monolithic color filter array based systems however provide this stability for imaging while maintaining registration as it is an inherent property of such devices.

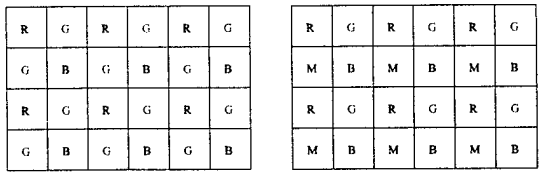

(a) (b)

Fig. 3. Bayer Color Filter Array (a)Classical form using three filters (b) Similar configuration with four filters

Commercially available Digital Still Color Cameras (DSCs) approach the problem of using a single sensor to capture multispectral data by making use of a monolithic array of color filters overlaid on a CCD array, such that each pixel records only one sample of the spectrum. Three or more different filters (typically three) are used in a tessellated fashion as shown in fig.3(a) [5]. To estimate say, a green pixel value at a location where a red sample was obtained, we interpolate (demosaic) and obtain this information from the neighbors. A variety of color filter array configurations are in use in DSCs. A few of these mosaics [6] are displayed in fig.4. The Bayer configuration is however the most commonly used.

We propose that mosaic technology is a robust alternative to existing multispectral imaging modalities, albeit with some loss in spatial resolution.

In Section 2 we illustrate commonly used demosaicking algorithms and compare their advantages and disadvantages. In section 3, we use experiments to illustrate the trade-off between gaining multispectral resolution over loss in spatial resolution due to mosaicking.

II. Demosaicking

An experiment equivalent to that done with mosaicking visible bands has not been done in the infrared (IR) or other spectral bands. Furthermore, it is interesting to note that we are not constrained to three bands or to conventional rectangular pixels or to the human visual system. For example, we could simply use the existing Bayer Array configuration and use four spectral bands instead of three as shown in fig.3(b). In fig.5(a), we illustrate a four-band hexagonal sampling arrangement for which we are currently building hardware. In this arrangement, each pixel has exactly two neighbors from each of the other bands.

In fig.5(b), we illustrate that seven bands can be sensed in this way. In this novel 7-band hexagonal arrangement, every pixel has exactly one adjacent neighbor in each band, so that the spectral intensity at any point can always be estimated from data no farther than one pixel away [7].

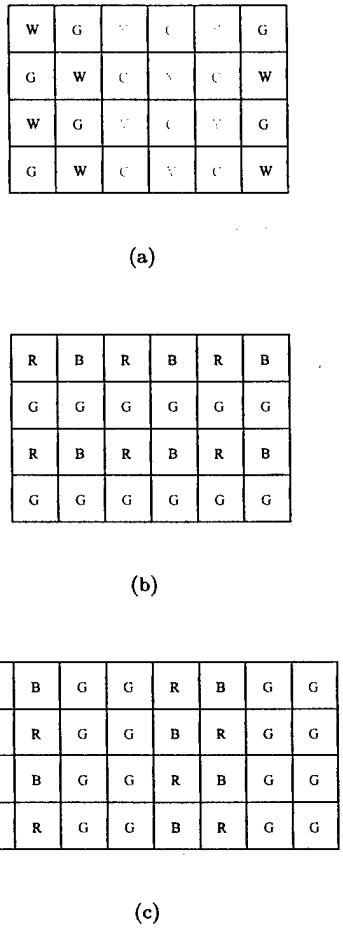

(a)

(b)

(c)

Fig. 4. Other Color Filter Arrays (a)Proposed by Yamanaka (b) Green channel along on alternate scan lines (c) another commonly used configuration

The choice of spectral bands chosen is entirely dependent upon the application.

The mosaic of samples is processed to produce a high resolution multispectral image such that the values of the color bands not sampled at a certain location are estimated from its neighbors. This process is often referred to as *demosaicking*. A variety of algorithms for demosaicking exist. The simplest one being bilinear interpolation. An exhaustive comparison of a some of the commonly used demosaicking methods is available in [8].

III. Experiments

In this section we compare results of demosaicking processes on different images using several different methods described in [9],[10],[11],[12] and [13]. These images should give the reader and idea about the pros and cons of this imaging modality, in each of the two types of images; those in the visible region and the IR region of the spectrum.

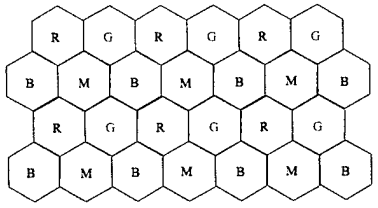

(a)

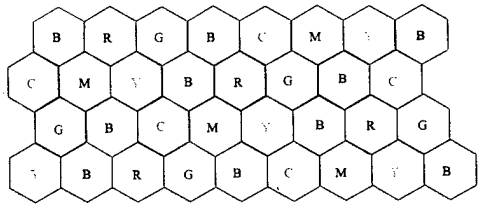

(b)

Fig. 5. Hexagonal configurations of color mosaics (a) Arrangement of four bandpass filters where each pixel has exactly two neighbors from other spectral bands (b) A similar arrangement in which seven spectral bands are measured, using seven filters, and a multispectral estimate may be obtained from immediate neighbors

The Mean Squared Error (MSE) is given by

$$MSE = \frac{1}{3MN}\sum_{k=1}^{3}\sum_{i,j=1}^{M,N}\Big(g(i,j,k) - f(i,j,k)\Big)^2 \qquad (1)$$

where $f(i,j,k)$ is the original image pixel intensity at pixel location (i,j) in band k and $g(i,j,k)$ is the estimated image pixel intensity at pixel location (i,j) in band k.

Although the MSE metric is not without limitations, especially when used as a global measure of image fidelity, it used due to its ease in implementation. We hence compare the algorithms with two different metrics, the first one being the mean squared error and the other, the ΔE^*_{ab} metric [14], which is the measured error in the $CIE-L^*a^*b^*$ color space, one of the many perceptually uniform color spaces. Errors in perceptually uniform color spaces measure errors that human observers perceive (which is meaningful for images in the visible spectrum).

A. Visible Spectrum

The images in the visible region of the spectrum were obtained using two different methods;

- simulation of the color filter array sampling for which we used data obtained from the hyperspectral Image dataset [15]. The results are presented in fig.6.
- a Pulnix TMC-1001 camera (outputs mosaicked images). Figs. 7 and 8 show results of demosaicking these images.

Table I shows the error metrics described above on these images. For the purposes of human viewing, image quality metrics in perceptually uniform color spaces or other metrics that measure image fidelity would be preferred for comparison.

In general, visible spectrum images have two kinds of errors,

- *zipper effect errors* that occur along intensity edges as seen in fig.7
- *confetti errors* that occur at isolated pixels that are at very high intensity compared to their neighbors, as seen in fig.8.

These errors are "disturbing" to a human observer when viewing color images of natural scenes or scenes about which humans have *prior knowledge.* Notice that the various algorithms have been developed with edge enhancement being the primary criterion. Images from left to right in fig.7 are in chronological order of development in this field.

B. IR Spectrum

The images in the IR region of the spectrum were obtained from the MASTER dataset [16] by subsampling the multispectral images using a Bayer sampling array. It is to be emphasized that this a simulation of multispectral mosaic imaging in IR. Mosaicked data obtained from a mosaicked IR sensor is not available at this time.

The results of demosaicking using algorithms devised for the visible spectrum are shown in fig.9. In general, we observe a similar trend in errors as found in visible spectrum images,

- *zipper effect errors*, that arise due to sharp intensity edges
- *confetti errors*, that arise due to the "low" spatial resolution of these images.

Satellite / airborne imagery has the inherent drawback that the images are of relatively poor resolution when compared to those of commercial available DSCs. This gives rise to confetti errors when rendered for human vision. However, it needs to be noted that these images are not to be viewed by an observer and appreciated for quality, rather these images will be used by target-seeking missles or parameter-monitoring systems which will use the spectral information in these images to perform recognition or other similar decision tasks. Multispectral capability is most useful when the targets are minimally resolved as is the case in satellite and airborne imagery. The bounds on "minimal" resolution are being researched and we hope to publish those results in the near future.

Table I shows average error metrics, averaged over different regions in these images. The Peak Signal to Noise ratio (PSNR) is given by

$$PSNR = 10log_{10}\frac{1}{MSE} \qquad (2)$$

where MSE is the mean squared error. The images are all scaled between 0 and 1.

We need to bear in mind that for decision-oriented or recognition systems, ROC curves would give a better measure of performance of these algorithms. But, due to the

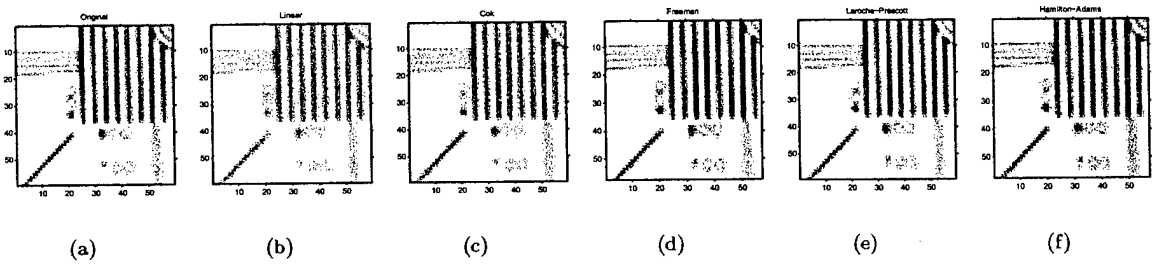

(a) (b) (c) (d) (e) (f)

Fig. 6. Simulation of DSC Images (a) Original Image (b)Linear Interpolation (c)Cok Interpolation (d)Freeman Interpolation (e) Laroche Interpolation (f)Hamilton-Adams Interpolation

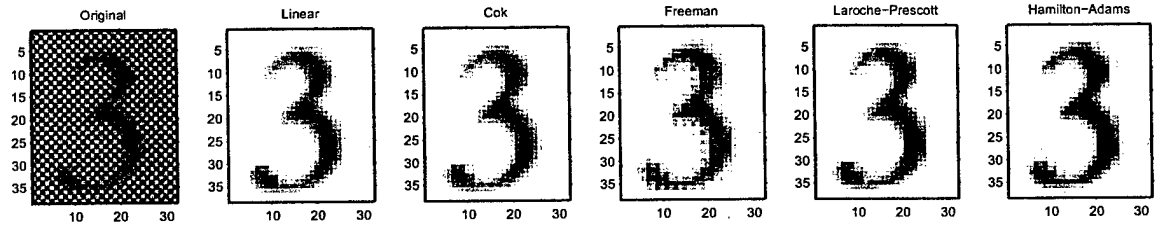

(a) (b) (c) (d) (e) (f)

Fig. 7. DSC Images illustrating zipper effect (a) Original Image (b)Linear Interpolation (c)Cok Interpolation (d)Freeman Interpolation (e) Laroche Interpolation (f)Hamilton-Adams Interpolation

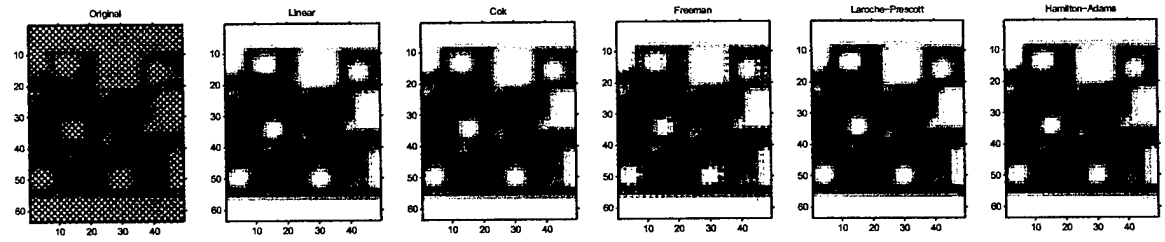

(a) (b) (c) (d) (e) (f)

Fig. 8. DSC Images illustrating confetti effect (a) Original Image (b)Linear Interpolation (c)Cok Interpolation (d)Freeman Interpolation (e) Laroche Interpolation (f)Hamilton-Adams Interpolation

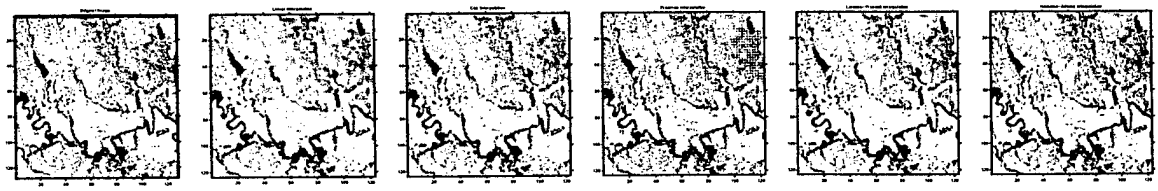

(a) (b) (c) (d) (e) (f)

Fig. 9. IR Image Mosaics; band 39(Red), 33(Green), 24(Blue) (a) Original Image (b)Linear Interpolation (c)Cok Interpolation (d)Freeman Interpolation (e) Laroche Interpolation (f)Hamilton-Adams Interpolation

wide applicability of this imaging modality, we restrict ourselves to the MSE metric.

IV. Conclusions

The errors quantified in table I give an idea about the performance of these algorithms. Clearly, Hamilton-

Algorithm used	Hyperspectral Image dataset			MASTER Images	
	ΔE^*_{ab}	ΔE_{RGB}	PSNR (dB)	MSE	PSNR (dB)
Linear	6.5766	0.0115	19.39	0.0570	12.92
Cok	3.1777	0.0024	26.19	0.0416	13.81
Freeman	2.5263	0.0011	29.59	0.0461	13.36
Laroche-Prescott	1.6681	0.00098	30.09	0.0410	13.87
Hamilton-Adams	1.2473	0.00045	33.48	0.0339	14.69

TABLE I

ERRORS FOR DIFFERENT INTERPOLATION ALGORITHMS ON THE HYPERSPECTRAL IMAGE DATA-SET AND MASTER IMAGES AFTER DEMOSAICKING

Adams' algorithm performs best under the MSE metric; which conforms to the visual appearance of the resulting images (the lowest ΔE^*_{ab} error, making the errors least detectable by a human observer) and is further corroborated by an increasing PSNR.

Although we "lost" spatial resolution in using the Bayer Array by using $\frac{1}{2}$ the number of green sensors and $\frac{1}{4}$ the number of red and blue sensors, we were able to reconstruct the full resolution images with good clarity, gaining

- robustness and
- the use of only one array of sensors.

Table II summarizes the advantages and disadvantages of this imaging modality.

	Multiple Sensors	Mosaicked Sensor Array
Registration	can be difficult	not required
Mechanical Robustness	sensitive	highly robust
No. of sensors for mxn size RGB images	mn R, mn G, mn B	$\frac{mn}{4}$ R, $\frac{mn}{2}$ G, $\frac{mn}{4}B$ (3-band Bayer)
No. of sensor arrays for 3 bands	3	1(3-band Bayer)
No. of sensor arrays for 7 bands	7	1(7-band Hexagonal)

TABLE II

PROS AND CONS OF MOSAICKING

Although there are performance bounds on the trade-off between loss in spatial resolution and the gain in spectral resolution, such a robust system has potential benefits far beyond other existing multispectral imaging systems for use in robotic, satellite-based, field-portable or hand-held systems.

The average loss observed by mosaicking sensors clearly suggests that the loss may be decreased by using "better" estimation / interpolation methods.

We are currently posing the process of demosaicking as an optimization problem with a cost function such that it minimizes the errors obtained due to mosaicking, using a variety of priors which will impose certain properties on the images while

- maximizing spectral overlap between observed target and "expected target". In other words, minimizing the "error" (however it be defined) between the observed and known spectral signatures of the target.
- maximizing probability of detection of the target (in ATR applications)

We anticipate presenting results of this work at the conference.

REFERENCES

[1] http://speclib.jpl.nasa.gov/, "Aster spectral library," 2000.

[2] K. Watson et. al., "Lithologic analysis from multispectral thermal infrared data of the alkalic rock complex at iron hill, colorado," *Jounal of the Society of Exploration Geophysicists*, vol. 61, May-June 1996.

[3] C.P. Lo, D.A. Quattrochi, and J.C. Luvall, "Application of high-resolution thermal infrared remote sensing and gis to assess the urban heat island effect," *International Journal of Remote Sensing*, 1997.

[4] P.E. Rybski et. al., "Enlisting rangers and scouts for reconnaissance and surveillance," *IEEE Robotics and Automation Magazine*, pp. 14–24, December 2000.

[5] B.E. Bayer, "Color imaging array," *United States Patent 3,971,065*, 1976.

[6] S. Yamanaka, "Solid state color camera," *United States Patent 4,054,906*, 1977.

[7] W.E. Snyder, "Invention disclosure," December 2000.

[8] R. Ramanath, "Interpolation methods for the bayer color array," M.S. thesis, North Carolina State University, Raleigh, NC 27695, 2000.

[9] J.E. Adams, "Design of practical color filter array interpolation algorithms for digital cameras," *Proc. SPIE, Real Time Imaging II*, vol. 3028, 1997.

[10] D. R. Cok, "Signal processing method and apparatus for producing interpolated chrominance values in a sampled color image signal," *United States Patent 4,642,678*, 1987.

[11] W. T. Freeman, "Median filter for reconstructing missing color samples," *United States Patent 4,724,395*, 1988.

[12] C.A. Laroche and M.A. Prescott, "Apparatus and method for adaptively interpolating a full color image utilizing chrominance gradients," *United States Patent 5,373,322*, 1994.

[13] J.F. Hamilton and J.E. Adams, "Adaptive color plan interpolation in single sensor color electronic camera," *United States Patent 5,629,734*, 1997.

[14] G. Wyszecki and W.S. Stiles, *Color Science – Concepts and Methods, Quantative Data and Formulae*, John Wiley and Sons, Inc., New York, second edition, 1982.

[15] D.H. Brainard, "Hyperspectral image data," .

[16] http://masterweb.jpl.nasa.gov, "Modis/aster data set," 2000.

Demosaicking methods for Bayer Color Arrays

Rajeev Ramanath[†] Wesley E. Snyder[†] Griff L. Bilbro[†] William Sander[‡]

Abstract

Digital Still Color Cameras sample the color spectrum using a monolithic array of color filters overlaid on a CCD array such that each pixel samples only one color band. The resulting mosaic of color samples is processed to produce a high resolution color image such that the values of the color bands not sampled at a certain location are estimated from its neighbors. This process is often referred to as *demosaicking*. This paper introduces and compares a few commonly used *demosaicking* methods using error metrics like mean squared error (MSE) in the RGB color space and perceived error in the *CIE-L*a*b** color space.

Index Terms

Demosaicking, Demosaicing, Color Filter Arrays, Digital Color Camera, DSC, Interpolation

I. Introduction

COMMERCIALLY available Digital Still Color Cameras (DSC) are based on a single CCD array and capture color information by using three or more color filters, each sample point capturing only one sample of the color spectrum. The Bayer Array [1] (shown in fig.1) is one of the many realizations of color filter arrays (CFA) possible. Many other implementations of a color-sampling grid have been incorporated in commercial cameras, most using the principle that the luminance channel (green) needs to be sampled at a higher rate than the chrominance channels (red and blue). The choice for green as "representative"

[†] Rajeev Ramanath, Wesley Snyder and Griff Bilbro are with the Department of Electrical and Computer Engineering at North Carolina State University, Raleigh, NC, 27695-7914, USA. Phone: (919) 513-2007, email: {*rramana, wes, glb*}*@eos.ncsu.edu*

[‡]William Sander is with the U.S. Army Research Office, Durham, P.O. Box 12211, Research Triangle Park, NC 27709, USA, Phone: (919) 529-4241, email: *sander@arl.aro.army.mil*

R_{11}	G_{12}	R_{13}	G_{14}	R_{15}	G_{16}	R_{17}
G_{21}	B_{22}	G_{23}	B_{24}	G_{25}	B_{26}	G_{27}
R_{31}	G_{32}	R_{33}	G_{34}	R_{35}	G_{36}	R_{37}
G_{41}	B_{42}	G_{43}	B_{44}	G_{45}	B_{46}	G_{47}
R_{51}	G_{52}	R_{53}	G_{54}	R_{55}	G_{56}	R_{57}
G_{61}	B_{62}	G_{63}	B_{64}	G_{65}	B_{66}	G_{67}
R_{71}	G_{72}	R_{73}	G_{74}	R_{75}	G_{76}	R_{77}

Fig. 1. Sample Bayer Pattern

of the luminance is due to the fact that the luminance response curve of the eye peaks at around the frequency of green light (see fig.2).

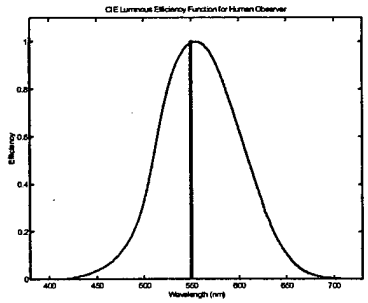

Fig. 2. Luminous Efficiency function of human observer. *Note: peak is at around frequency of green light*

Since, at each pixel, only one spectral measurement was made, the other colors must be estimated using information from all the color planes in order to obtain a high resolution color image. This process is often referred to as *demosaicking*. Interpolation must be performed on the mosaicked image data. There are a variety of methods available, the simplest being linear interpolation, which, as shall be shown, does not maintain edge information well. More complicated methods [2], [3], [4], [5], [6] perform this interpolation and attempt to maintain edge detail or limit *hue* transitions. In [7], Trussell introduces a linear lexicographic model for the image formation and demosaicking process, which may be used in a reconstruction step. In [8], linear response models proposed by Vora et.al [9] have been used to reconstruct

these mosaicked images using an optimization technique called Mean Field Annealing [10]. In this paper we briefly describe the more commonly used demosaicking algorithms and demonstrate their strengths and weaknesses. In Section II, we describe the interpolation methods we use in our comparisons. We compare the interpolation methods by running the algorithms on three types of images (two types of synthetic image sets and one set of real-world mosaicked images). The images used for comparison and their properties are presented in section III. Qualitative and quantitative results are presented in Section IV. Discussions about the properties of these algorithms and their overall behavior are presented in Section V. We use two error metrics, the mean squared error in the RGB color space and the ΔE^*_{ab} error in the *CIE-$L^*a^*b^*$* color space (described in the Appendix).

II. Demosaicking Strategies

A. Ideal Interpolation

Sampling of a continuous image $f(x,y)$ yields infinite repetitions of its continuous spectrum $F(\zeta,\eta)$ in the Fourier domain. If these repetitions do not overlap (which is almost never the case as natural images are not band-limited), the original image $f(x,y)$ can be reconstructed exactly from its discrete samples $f(m,n)$, otherwise we observe the phenomenon of aliasing. The 1-D "ideal" interpolation is the multiplication with a *rect* function in the frequency domain and can be realized in the spatial domain by a convolution with the *sinc* function. This "ideal interpolator" kernel is band-limited and hence is not space limited. It is primarily of theoretical interest and not implemented in practice [11].

B. Neighborhood considerations

It may be expected that we get better estimates for the missing sample values by increasing the neighborhood of the pixel, but this increase is computationally expensive. There

is hence a need to keep the interpolation filter kernel space-limited to a small size and also extract as much information from the neighborhood as possible. To this end, correlation between color channels is used [12]. For RGB images, cross-correlation between channels has been determined and found to vary between 0.25 and 0.99 with averages of 0.86 for red/green, 0.79 for red/blue and 0.92 for green/blue cross correlations [13]. One well-known image model [12] is to simply assume that red and blue are perfectly correlated with the green over a small neighborhood and thus differ from green by only an offset. This image model is given by

$$G_{ij} = R_{ij} + k \tag{1}$$

where (i, j) refers to the pixel location, R (known) and G (unknown) the red and green pixel values, k is the appropriate bias for the given pixel neighborhood. The same applies at a blue pixel location. Let us illustrate eqn.1 with an example by considering the green channel of an image and the corresponding Green minus Red and Green minus Blue channels. In fig.3, we can see that majority of the regions in the Green minus Red and Green minus Blue images are locally uniform (the constant k in eqn.1), especially in regions where there is high spatial detail (near the eyes of the macaws, say).

Hence the choice of the neighborhood size is critical. It is observed that most implementations are designed with hardware implementation in mind (paying great attention to the need for pipelining, system latency and throughput per clock cycle). The larger the neighborhood, the greater the difficulty in pipelining, the greater the latency, and possibly, lesser the throughput.

C. Bilinear Interpolation

Consider the array of pixels as shown in fig.1. At a blue center (where blue color was measured), we need to estimate the green and red components. Consider pixel location 44

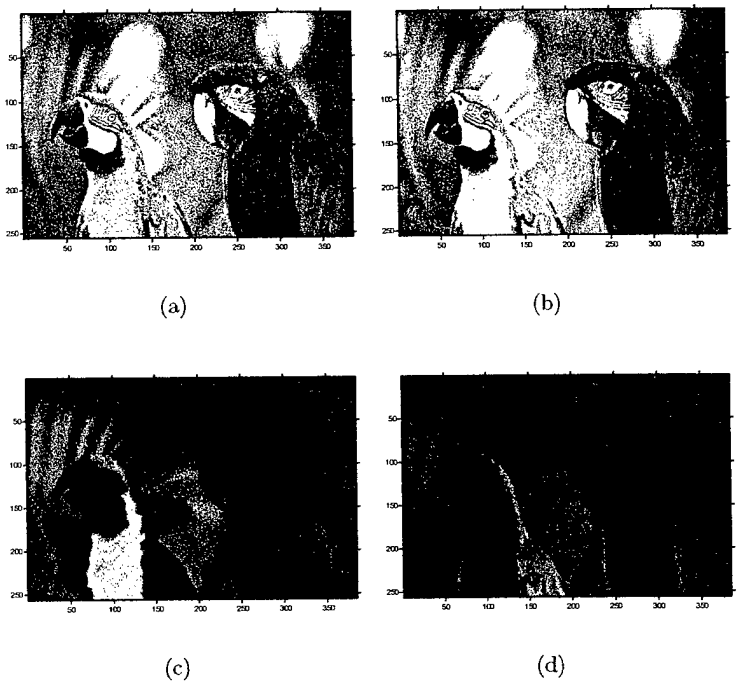

Fig. 3. (a) RGB image b) Green Channel c) Green minus Red (d)Green minus Blue

at which only B_{44} is measured; we need to estimate G_{44}. Given G_{34}, G_{43}, G_{45}, G_{54}, one estimate for G_{44} is given by $G_{44} = (G_{34} + G_{43} + G_{45} + G_{54})/4$. To determine R_{44}, given R_{33}, R_{35}, R_{53}, R_{55}, the estimate for R_{44} is given by $R_{44} = (R_{33} + R_{35} + R_{53} + R_{55})/4$. At a red center, we would estimate the blue and green accordingly. Performing this process at each photo-site (location on the CCD), we can obtain three color planes for the scene which would give us one possible demosaicked form of the scene.

The band-limiting nature of this interpolation smooths edges, which shows up in color images as fringes (referred to as the *zipper* effect [12], [14]). This has been illustrated with two colors channels (for simplicity) in fig.4.

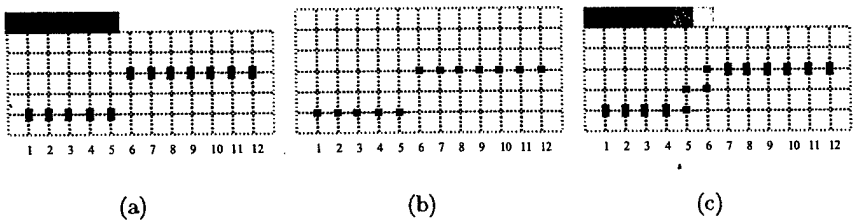

Fig. 4. Illustration of fringe or zipper effect resulting from the linear interpolation process. An edge is illustrated as going from navy blue (0,0,128) to yellow (255,255,128). The zipper effect produces green pixels near the edge (a) Original image (only 2 colors, blue constant at 128) (b) one scan line of subsampled Bayer pattern (choose every other pixel) (c) result of estimating missing data using linear interpolation. *Observe color fringe in locations 5 and 6*

D. Constant hue-based Interpolation

In general, *hue* is defined as the property of colors by which they can be perceived as ranging from red through yellow, green, and blue, as determined by the dominant wavelength of the light. Constant hue-based Interpolation, proposed by Cok [2] and is one of the first few methods used in commercial camera systems. Modifications of this system are still in use. The key objection to pixel artifacts in images that result from bilinear interpolation is abrupt and unnatural hue change [2]. There is a need to maintain the hue of the color such that there are no sudden jumps in hue (except for over edges, say). The red and blue channels are assigned to be the chrominance channels while the green channel is assigned as the luminance channel.

As used in this section, *hue* is defined by a vector of ratios as $(R/G, B/G)$ [2]. It is to be noted that the term hue defined above is valid for this method only, also, the hue needs to be "redefined" if the denominator G is zero. By interpolating the hue value and deriving the interpolated chrominance values (blue and red) from the interpolated hue values, *hues* are allowed to change only gradually, thereby reducing the appearance of color fringes which would have been obtained by interpolating only the chrominance values.

Consider an image with constant hue. In exposure space (be it logarithmic[1] or linear), the values of the luminance (G) and one chrominance component (R, say) at a location (i,j) and a neighboring sample location (k,l) are related as $R_{ij}/R_{kl} = G_{ij}/G_{kl}$ if $B_{ij}/B_{kl} = G_{ij}/G_{kl}$.

If R_{kl} represents the unknown chrominance value, and R_{ij} and G_{ij} represent measured values and $\boldsymbol{G_{kl}}$ represents the interpolated luminance value, the missing chrominance value R_{kl} is given by $R_{kl} = \boldsymbol{G_{kl}}(R_{ij}/G_{ij})$ In an image that does not have uniform hue, as in a typical color image, smoothly changing *hues* are assured by interpolating the hue values between neighboring chrominance values.

The green channel is first interpolated using bilinear interpolation. After this first pass, the hue is interpolated. Referring to fig.1,

$$R_{44} = \boldsymbol{G_{44}} \frac{\frac{R_{33}}{\boldsymbol{G_{33}}} + \frac{R_{35}}{\boldsymbol{G_{35}}} + \frac{R_{53}}{\boldsymbol{G_{53}}} + \frac{R_{55}}{\boldsymbol{G_{55}}}}{4} \tag{2}$$

and similarly for the blue channel

$$B_{33} = \boldsymbol{G_{33}} \frac{\frac{B_{22}}{\boldsymbol{G_{22}}} + \frac{B_{24}}{\boldsymbol{G_{24}}} + \frac{B_{42}}{\boldsymbol{G_{42}}} + \frac{B_{44}}{\boldsymbol{G_{44}}}}{4} \tag{3}$$

The G values in bold-face are estimated values, after the first pass of interpolation. The extension to the logarithmic exposure space is straightforward as multiplications and divisions in the linear space become additions and subtractions, respectively in the logarithmic space. There is a caveat however as interpolations will be performed in the logarithmic space and hence the relations in linear space and exposure space are not identical [2]. Hence in most implementations the data is first linearized [15] and then interpolated as described above.

[1] Most cameras capture data in a logarithmic exposure space and need to be linearized before the ratios used as such. If interpolating in the logarithmic exposure space, difference of logarithms needs to be taken instead of ratios; i.e. $\log(R_{ij}/R_{kl}) = \log(R_{ij}) - \log(R_{kl})$

E. Median-based Interpolation

This method, proposed by Freeman [3], is a two pass process, the first being a linear interpolation, and the second pass a median filter of the color differences.

In the first pass, linear interpolation is used to populate each photo-site with all three colors and in the second pass, the difference image, of say, Red minus Green and Blue minus Green is median filtered. The median filtered image thus obtained is then used in conjunction with the original Bayer array samples to recover the samples (illustrated below). This method preserves edges very well, as illustrated in fig.5 where only one row of the Bayer array is considered since this process can be extrapolated to the case of the rows containing blue and green pixels. Fig.5(a) shows one scan line of the original image before Bayer subsampling, the horizontal axis is the location index and the vertical axis represents intensity of red and green pixels. We have a step edge between locations 5 and 6. Fig.5(b) shows the same scan line, sampled in a Bayer fashion, picking out every other pixel for red and green. Fig.5(c) (step 1 of this algorithm) shows the result of estimating the missing data using linear interpolation. Notice the color fringes introduced between pixel locations 5 and 6; fig.5(d) (step 2) shows the absolute valued difference image between the two channels; fig.5(e) (step 3) shows the result of median filtering the difference image with a kernel of size 5. Using this result and the sampled data, fig.5(f) is generated (step 4) as an estimate of the original image (by adding the median filtered result to the sampled data, *e.g.* the red value at location 6 is estimated by adding the median filtered result at location 6 to the sampled green value at location 6). The reconstruction of the edge in this example is exact, although note that for a median filter of size 3, this will not be the case.

This concept can be carried over to three color sensors wherein differences are calculated between pairs of colors and the median filter is applied to these differences to generate the

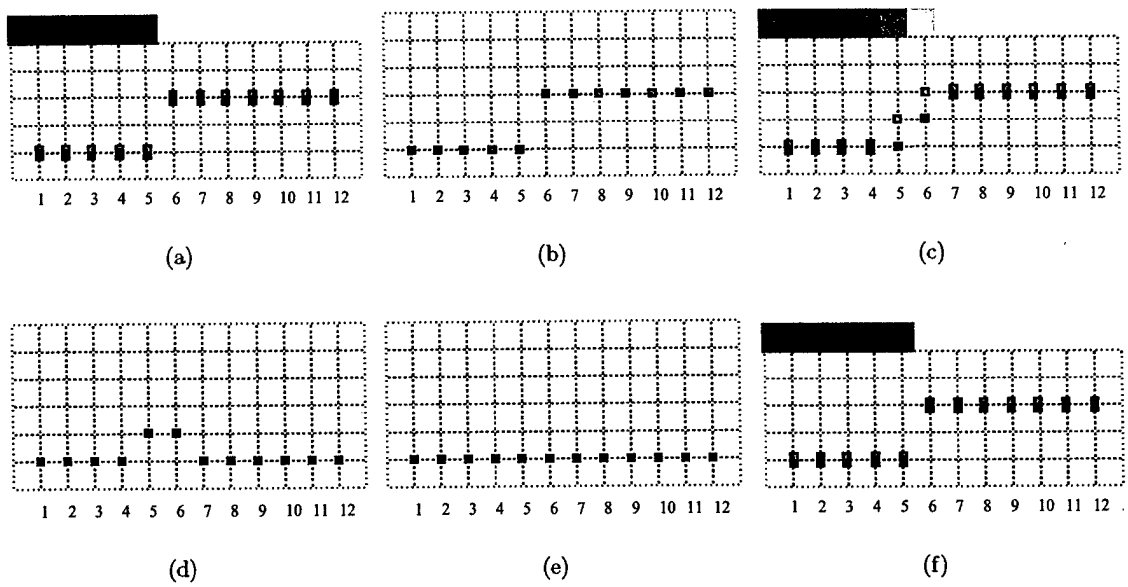

Fig. 5. Illustration of Freeman's interpolation method for a two channel system, as in fig.4 an edge is illustrated as going from navy blue (0,0,128) to yellow (255,255,128) (a) Original image (only 2 colors, blue constant at 128) (b) one scan line of subsampled Bayer pattern (choose every other pixel) (c) result of linear interpolation (d) Green minus Red (e) median filtered result of the difference image (f) reconstructed image

final image.

We shall consider neighborhoods of a size such that all the algorithms can be compared on the same basis. The algorithms described in this document have at most 9 pixels under consideration for "estimation". In a square neighborhood, this would imply a 3 x 3 window. We shall hence use a 3 x 3 neighborhood for Freeman's algorithm.

F. Gradient Based Interpolation

This method was proposed by Laroche and Prescott [4] and is in use in the Kodak DCS 200 Digital Camera System. It employs a three step process, the first one being the interpolation of the luminance channel (green) and the second and third being interpolation of the color differences (red minus green and blue minus green). The interpolated color differences are used to reconstruct the chrominance channels (red and blue). This method

takes advantage of the fact that the human eye is most sensitive to luminance changes. The interpolation is performed depending upon the position of an edge in the green channel. Referring to fig.1, if we need to estimate G_{44}, let $\alpha = \text{abs}\big((B_{42}+B_{46})/2 - B_{44}\big)$ and $\beta = \text{abs}\big((B_{24}+B_{64})/2 - B_{44}\big)$. We refer to α and β as "classifiers" and will use them to determine if a pixel belongs to a vertical or horizontal edge, respectively. It is intriguing to note that the classifiers used are second derivatives with the sign inverted and halved in magnitude. We come up with the following estimates for the missing green pixel value.

$$\boldsymbol{G_{44}} = \begin{cases} \dfrac{G_{43}+G_{45}}{2} & \text{if} \quad \alpha < \beta \\ \dfrac{G_{34}+G_{54}}{2} & \text{if} \quad \alpha > \beta \\ \dfrac{G_{43}+G_{45}+G_{34}+G_{54}}{4} & \text{if} \quad \alpha = \beta \end{cases} \tag{4}$$

Similarly, for estimating G_{33}, let $\alpha = \text{abs}\big((R_{31}+R_{35})/2 - R_{33}\big)$ and $\beta = \text{abs}\big((R_{13}+R_{53})/2 - R_{33}\big)$. These are estimates to the horizontal and vertical second derivatives in red, respectively. Using these gradients as classifiers, we come up with the following estimates for the missing green pixel value.

$$\boldsymbol{G_{33}} = \begin{cases} \dfrac{G_{32}+G_{34}}{2} & \text{if} \quad \alpha < \beta \\ \dfrac{G_{23}+G_{43}}{2} & \text{if} \quad \alpha > \beta \\ \dfrac{G_{32}+G_{34}+G_{23}+G_{43}}{4} & \text{if} \quad \alpha = \beta \end{cases} \tag{5}$$

Once the luminance is determined, the chrominance values are interpolated from the differences between the color (red and blue) and luminance (green) signals. This is given by

$$\begin{aligned} R_{34} &= \frac{(R_{33}-\boldsymbol{G_{33}})+(R_{35}-\boldsymbol{G_{35}})}{2} + G_{34} \\ R_{43} &= \frac{(R_{33}-\boldsymbol{G_{33}})+(R_{35}-\boldsymbol{G_{35}})}{2} + G_{43} \\ R_{44} &= \frac{(R_{33}-\boldsymbol{G_{33}})+(R_{35}-\boldsymbol{G_{35}})+(R_{53}-\boldsymbol{G_{53}})+(R_{55}-\boldsymbol{G_{55}})}{4} + G_{44} \end{aligned} \tag{6}$$

Note that the green channel has been completely estimated before this step. The bold-face entries correspond to estimated values. We get corresponding formulae for the blue pixel locations. Interpolating color differences and adding the green component has the advantage of maintaining color information and also using intensity information at pixel locations. At this point, three complete RGB planes are available for the full resolution color image.

G. Adaptive Color Plan Interpolation

This method is proposed by Hamilton and Adams [5]. It is a modification of the method proposed by Laroche and Prescott [4]. This method also employs a multiple step process, with classifiers similar to those used in Laroche-Prescott's scheme but modified to accommodate first order and second order derivatives. The estimates are composed of arithmetic averages for the chromaticity (red and blue) data and appropriately scaled second derivative terms for the luminance (green) data. Depending upon the preferred orientation of the edge, the predictor is chosen. This process also has three runs. The first run populates that luminance (green) channel and the second and third runs populate the chrominance (red and blue) channels.

Consider the Bayer array neighborhood shown in fig.6(a). G_i is a green pixel and A_i is either a red pixel or a blue pixel (All A_i pixels will be the same color for the entire neighborhood). We now form classifiers $\alpha = \text{abs}(-\boldsymbol{A_3} + \boldsymbol{2A_5} - \boldsymbol{A_7}) + \text{abs}(G_4 - G_6)$ and $\beta = \text{abs}(-\boldsymbol{A_1} + \boldsymbol{2A_5} - \boldsymbol{A_9}) + \text{abs}(G_2 - G_8)$. These classifiers are composed of second derivative terms for chromaticity data and gradients for the luminance data. As such, these classifiers sense the high spatial frequency information in the pixel neighborhood in the horizontal and vertical directions.

Consider, that we need to estimate the green value at the center, i.e. to estimate G_5.

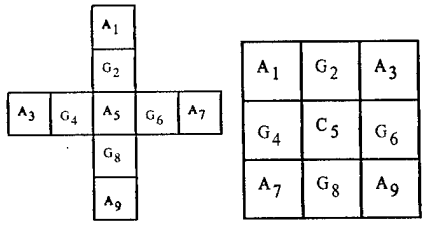

(a) (b)

Fig. 6. Sample Bayer Neighborhood, A_i = Chrominance (blue / red), G_i = Luminance, C_5 = red / blue

Depending upon the preferred orientation, the interpolation estimates are determined as

$$\boldsymbol{G_5} = \begin{cases} \dfrac{G_4+G_6}{2} + \dfrac{-A_3+2A_5-A_7}{2} & \text{if } \alpha < \beta \\ \dfrac{G_2+G_8}{2} + \dfrac{-A_1+2A_5-A_9}{2} & \text{if } \alpha > \beta \\ \dfrac{G_2+G_4+G_6+G_8}{4} + \dfrac{-A_1-A_3+4A_5-A_7-A_9}{8} & \text{if } \alpha = \beta \end{cases} \tag{7}$$

These predictors are composed of arithmetic averages for the green data and appropriately scaled second derivative terms for the chromaticity data. This comprises the first pass of the interpolation algorithm. The second pass involves populating the chromaticity channels. Consider the neighborhood as shown in fig.6(b). G_i is a green pixel and A_i is either a red pixel of a blue pixel and C_i is the opposite chromaticity pixel. Then $A_2 = (A_1+A_3)/2 + (-\boldsymbol{G_1} + 2G_2 - \boldsymbol{G_3})/2$, $A_4 = (A_1+A_7)/2 + (-\boldsymbol{G_1} + 2G_4 - \boldsymbol{G_7})/2$. These are used when the nearest neighbors to A_i are in the same row and column respectively.

To estimate C_5, we employ the same method as we did to estimate the luminance channel. We again, form two classifiers, α and β which "estimate" the gradient in the horizontal and vertical directions. $\alpha = \text{abs}(-\boldsymbol{G_3} + \boldsymbol{2G_5} - \boldsymbol{G_7}) + \text{abs}(A_3 - A_7)$ and $\beta = \text{abs}(-\boldsymbol{G_1} + \boldsymbol{2G_5} - \boldsymbol{G_9}) + \text{abs}(A_1 - A_9)$. α and β "sense" the high frequency information in the pixel neighborhood in the positive and negative diagonal respectively. We now have

estimates

$$C_5 = \begin{cases} \dfrac{A_3 + A_7}{2} + \dfrac{-G_3 + 2G_5 - G_7}{2} & \text{if } \alpha < \beta \\ \dfrac{A_1 + A_9}{2} + \dfrac{-G_1 + 2G_5 - G_9}{2} & \text{if } \alpha > \beta \\ \dfrac{A_1 + A_3 + A_7 + A_9}{4} + \dfrac{-G_1 - G_3 + 4G_5 - G_7 - G_9}{4} & \text{if } \alpha = \beta \end{cases} \quad (8)$$

These estimates are composed of arithmetic averages for the chromaticity data and appropriately scaled second derivative terms for the green data. Depending upon the preferred orientation of the edge, the predictor is chosen. We now have the three color planes populated for the Bayer Array data.

III. Comparison of Interpolation Methods

We generated test images, shown in fig.7 and fig.8 which are simulations of the data contained in the Bayer Array of the camera. In other words, these are images that consider "what-if" cases in the Bayer Array. They were chosen as test images to emphasize the various details that each algorithm works on.

A. Type I Test Images

Images of this type are synthetic and have edge orientations along both the cardinal directions as well as in arbitrary directions as shown in fig.7. Test Image_1 was chosen to demonstrate the artifacts each process introduces for varying thicknesses of stripes (increasing spatial frequencies). Test Image_2 was chosen to study a similar performance, but with a constant spatial frequency. Test Image_3 is a section from the starburst pattern, to test the robustness of these algorithms for non-cardinal edge orientations. *Note that these images have perfectly correlated color planes. The intent of these images is to highlight alias-induced fringing errors.*

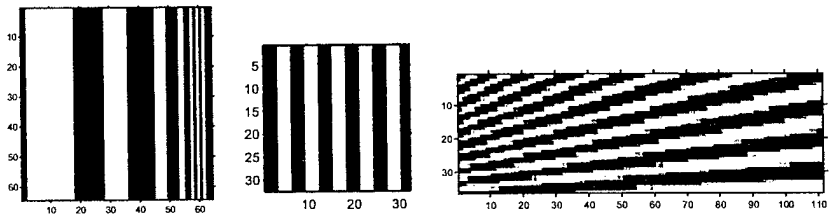

(a) (b) (c)

Fig. 7. Type I Test Images, a) Test Image$_1$ has vertical bars with decreasing thicknesses(16 pixels down to 1 pixel) b) Test Image$_2$ has bars of constant width (3 pixels) (c) Test Image$_3$ is a section from the starburst pattern

B. Type II Images

Three RGB images, shown in fig.8 were subsampled in the form of a Bayer array and then interpolated to get the three color planes. The regions of interest (ROIs) in this image has been highlighted with a white box. These images were chosen specifically to highlight

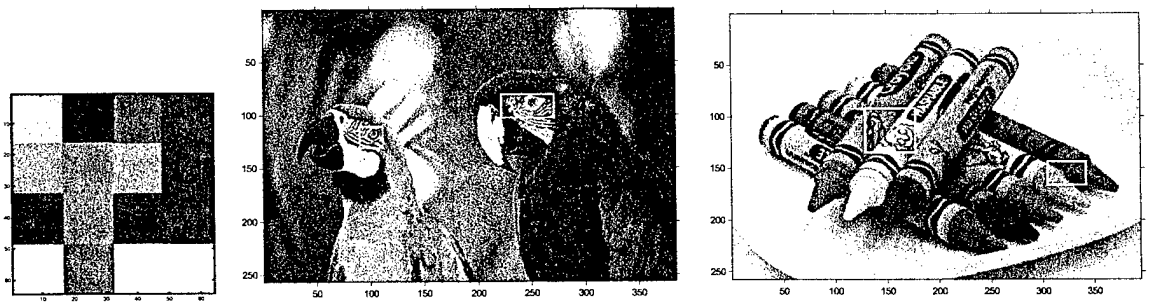

(a) (b) (c)

Fig. 8. Type II Images, (a) Test Image$_4$ (b) Original RGB Macaw Image showing ROIs (c) Original Crayon Image showing ROIs

the behavior of these algorithms when presented with color edges. Test Image$_4$ is a synthetic image of randomly chosen color patches. Unlike Type I images, these images have sharp discontinuities in all color planes, independent of each other. The ROIs in fig.8(b) have relatively high spatial frequencies. The ROIs in fig.8(c) have distinct color edges, one between

pastel colors and the other between fully saturated colors.

C. Type III Images

This category of images consists of real-world camera images captured with a camera that has a CFA pattern. No internal interpolation is performed on them. We were therefore able to get the "true" CFA imagery corrupted only by the optical PSF. The ROIs of these images are shown in figs.17(a) and 18(a). CFA_1 has sharp edges and high frequency components while CFA_2 has a color edge.

IV. Results

The results of the demosaicking algorithms presented in section II on the three types of images are shown in figs.9 to 18. Literature [16] suggests that the ΔE^*_{ab} (definition included in the Appendix) error metric represents human perception effectively. We hence make use of this to quantify the errors observed. However, bear in mind the bounds on this error for detectability that ΔE^*_{ab} errors less than about 2.3 are not easily detected while on the other hand, errors greater than about 10 are so large that relative comparison is insignificant [17]. This metric gives us a measure of the difference between colors as viewed by a standard observer. Another metric used for comparison is the mean squared error (MSE) which provides differences between colors in a "Euclidean" sense. MSE, although not being representative of the errors we perceive, is popular because of its tractability and ease in implementation. These metrics are tabulated in Tables I and II. The boldface numbers represent the minimum values in the corresponding image, which gives us an idea about which algorithm performs best for a given image. *There will be errors introduced in the printing/reproduction process, but assuming that the errors will be consistent for all the reproductions, we may infer relative performance of these algorithms.*

In fig.9 and fig.10, notice the fringe artifacts introduced in linear interpolation, termed as the *zipper* effect by Adams [12]. The appearance of this effect is considerably reduced (observe the decrease in the metrics) in Cok's interpolation. Hamilton-Adams' and Laroche-Prescott's implementation estimates Test Image$_2$ exactly (notice that the MSE and ΔE^*_{ab} errors are zero). This is because both these algorithms use information from the other channels for estimation (chrominance channel to interpolate luminance and vice versa). Notice that all these algorithms perform poorly at high spatial frequencies. All the algorithms discussed here have identical properties in the horizontal and vertical directions.

For non-cardinal edge orientations such as those shown in Test Image$_3$ (fig.11) performance (observed in the error metrics also) is noted to be worse. Note that the ΔE^*_{ab} error metric is "on an average" considerably higher for Test Image$_3$ when compared to Test Image$_1$ and Test Image$_2$.

Algorithm used	**Test Image$_1$**	**Test Image$_2$**	**Test Image$_3$**	**Test Image$_4$**	**Macaw ROI$_1$**	**Macaw ROI$_2$**	**Crayon ROI$_1$**	**Crayon ROI$_2$**
Linear	34.731	65.487	57.553	9.711	15.457	23.299	7.293	3.645
Cok	16.352	27.122	30.828	11.437	11.017	14.924	6.003	4.131
Freeman	15.179	55.301	**19.513**	9.599	**5.404**	**7.421**	4.649	**3.645**
Laroche-Prescott	7.321	0	24.592	10.944	11.028	14.198	5.507	4.234
Hamilton-Adams	**3.052**	0	21.793	**9.303**	9.279	11.579	**4.409**	3.936

TABLE I

ΔE^*_{ab} ERRORS FOR DIFFERENT INTERPOLATION ALGORITHMS AFTER DEMOSAICKING

Test Image$_4$ has been used to illustrate the performance of these algorithms when presented with sharp edges which do not have correlated color planes (see fig.12. From the error metrics, it is clear that all of them perform poorly at sharp color edges. Note however that although the ΔE^*_{ab} errors are high, the squared error metric is relatively low, clearly highlighting the advantage of using ΔE^*_{ab}. Using only the squared error would have been

Algorithm used	Test Image_1	Test Image_2	Test Image_3	Test Image_4	Macaw ROI_1	Macaw ROI_2	Crayon ROI_1	Crayon ROI_2
Linear	154	253	101.6	**18.1**	33.0	68.6	10.4	1.7
Cok	100	163	67.3	31.0	20.5	37.5	6.7	2.1
Freeman	52.2	134	**5.7**	19.9	**3.9**	**3.4**	**2.8**	**1.6**
Laroche-Prescott	35.3	0	8.8	26.2	20.1	31.5	5.8	1.9
Hamilton-Adams	**21.4**	0	8.3	26.6	11.7	10.5	3.3	1.9

TABLE II

MSE (x 10^{-3}) FOR DIFFERENT INTERPOLATION ALGORITHMS AFTER DEMOSAICKING

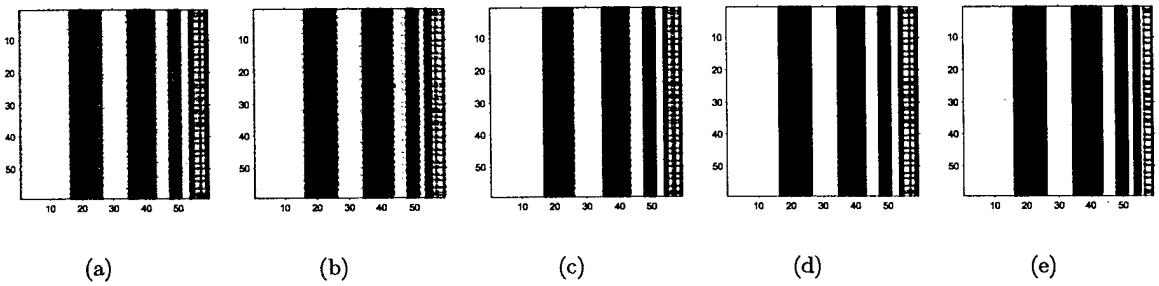

Fig. 9. (a)Linear (b)Cok (c)Freeman (d)Laroche-Prescott (e)Hamilton-Adams interpolations on Test Image_1. *Note: Images are not the same size as original. Image has been cropped to hide edge effects*

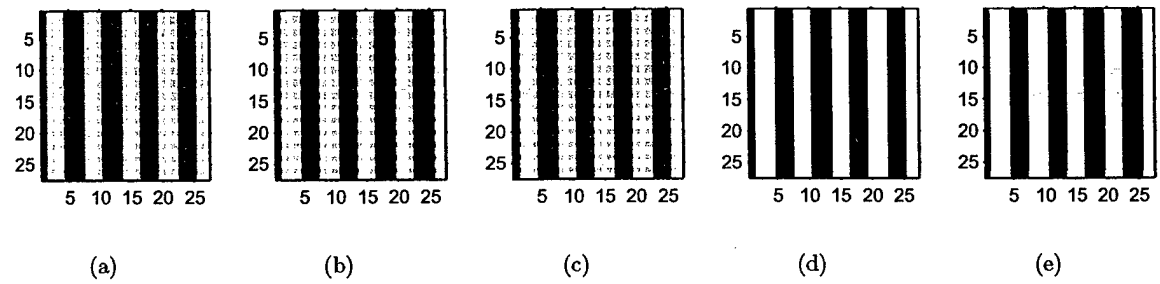

Fig. 10. (a)Linear (b)Cok (c)Freeman (d)Laroche-Prescott (e)Hamilton-Adams interpolations on Test Image_2. *Note: Images are not the same size as original. Image has been cropped to hide edge effects*

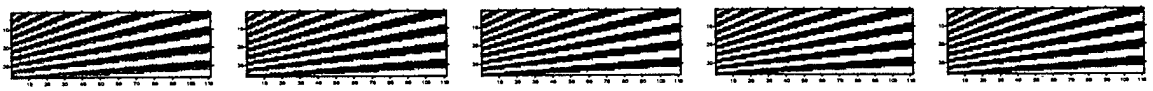

(a) (b) (c) (d) (e)

Fig. 11. (a)Linear (b)Cok (c)Freeman (d)Laroche-Prescott (e)Hamilton-Adams interpolations on Test Image_3. *Note: Images are not the same size as original. Image has been cropped to hide edge effects*

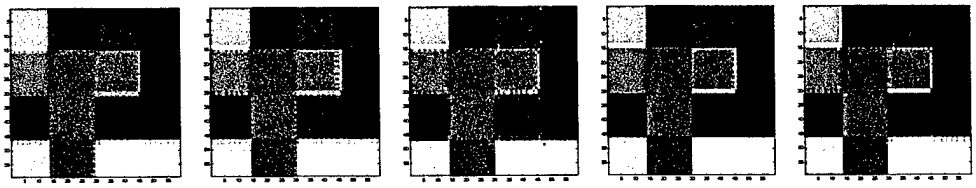

(a) (b) (c) (d) (e)

Fig. 12. (a)Linear (b)Cok (c)Freeman (d)Laroche-Prescott (e)Hamilton-Adams interpolations on Test Image_4. *Note: Images are not the same size as original. Image has been cropped to hide edge effects*

misleading.

The macaw images illustrate the alias-induced errors while at the same time, showing a *confetti* type of error. These errors come about due to intensely bright or dark points (in a dark or bright neighborhood, respectively). Freeman's algorithm performs best in these regions because it is able to remove such "speckle" behavior in the images due to the median filtering process (observe that the ΔE^*_{ab} errors are smallest for Freeman's algorithms in such regions).

The crayon images on the other hand are reproduced very precisely (see fig.15 and fig.16), with very few errors. ROI_1 shows some errors at the edges where the line-art appears. However, this error is not very evident. ROI_2 is reproduced almost exactly. In fact, depending upon the print process or the display rendering process, one may not be able to see the errors generated at all. This shows that these algorithms perform very well at blurred color edges (which is the case with many natural scenes).

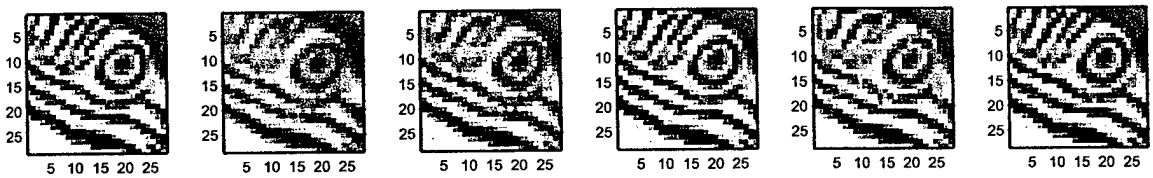

(a) (b) (c) (d) (e) (f)

Fig. 13. (a) Original "truth" ROI_1 of macaw image (b)Linear (c)Cok (d)Freeman (e)Laroche-Prescott (f)Hamilton-Adams interpolations on Macaw Image. *Note: Images are displayed along with original image for comparison purposes*

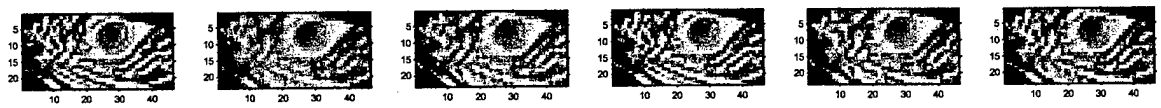

(a) (b) (c) (d) (e) (f)

Fig. 14. (a) Original "truth" ROI_2 of macaw image (b)Linear (c)Cok (d)Freeman (e)Laroche-Prescott (f)Hamilton-Adams interpolations on Macaw Image. *Note: Images are displayed along with original image for comparison purposes*

In Type III images which are raw readouts from a CFA camera, we cannot use the metrics we have been using thus far as there is no "reference" image with which to compare these results. However we may use visual cues to determine performance, and we observe similar trends in these images as was observed in synthetic images. Observe in fig.17 that the high spatial frequencies and non-cardinal edge orientations are not reproduced correctly (as was the case with Type I images). Color edges are also reproduced with reasonably good fidelity as is seen in fig.18 - although some *zipper* effect is observed with Linear and Cok interpolations.

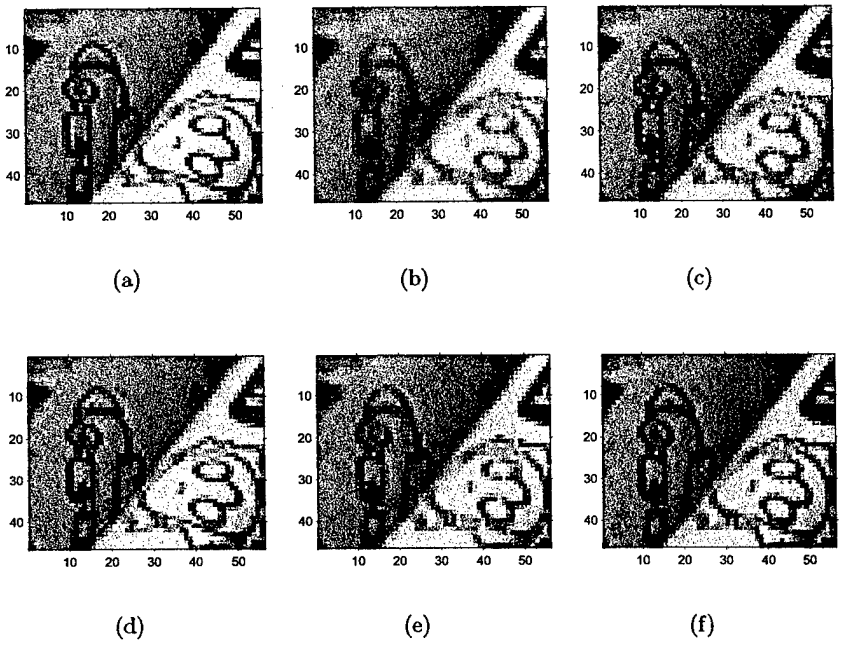

Fig. 15. (a) Original "truth" ROI_1 of crayon image (b)Linear (c)Cok (d)Freeman (e)Laroche-Prescott (f)Hamilton-Adams interpolations on Macaw Image. *Note: Images are displayed along with original image for comparison purposes*

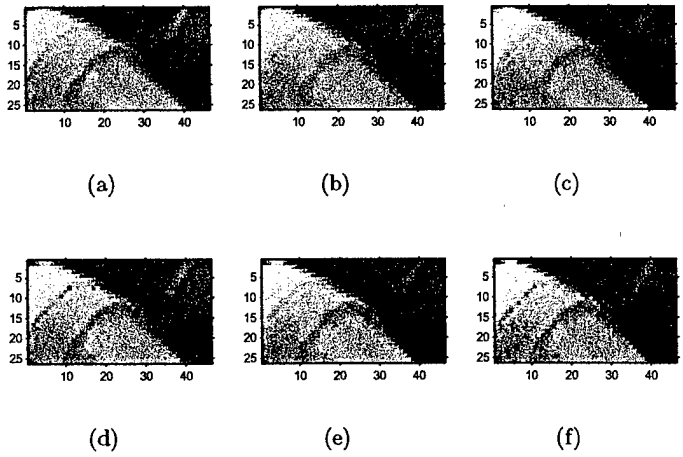

Fig. 16. (a) Original "truth" ROI_2 of crayon image (b)Linear (c)Cok (d)Freeman (e)Laroche-Prescott (f)Hamilton-Adams interpolations on Macaw Image. *Note: Images are displayed along with original image for comparison purposes*

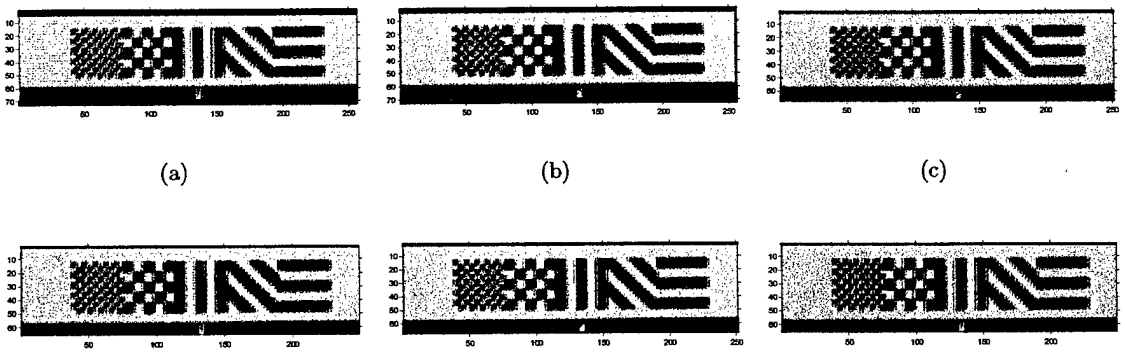

(a) (b) (c)

(d) (e) (f)

Fig. 17. (a) Original image CFA_1 (b)Linear (c)Cok (d)Freeman (e)Laroche-Prescott (f)Hamilton-Adams interpolations

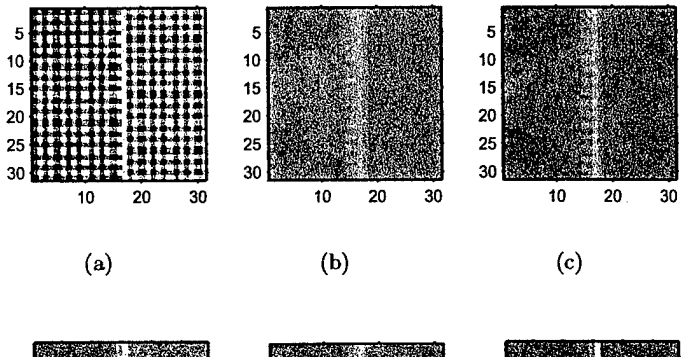

(a) (b) (c)

(d) (e) (f)

Fig. 18. (a) Original image CFA_2 (b)Linear (c)Cok (d)Freeman (e)Laroche-Prescott (f)Hamilton-Adams interpolations

V. Discussion

Laroche-Prescott's and Hamilton-Adams' interpolation processes have similar forms. Both of them use second derivatives to perform interpolation which may be written as

$$v = u + \lambda g \tag{9}$$

where u is the data (original image), v is the resulting image $\lambda > 0$, g is a suitably defined gradient. We may think of eqn.9 in the form of that used for unsharp masking [18], an enhancement process. Unsharp masking may be interpreted as either subtraction of the low-pass image from the original image (scaled) or of even as addition of a high-pass image to the original image (scaled). To see the equivalence let the image I be written as

$$I = L + H \tag{10}$$

the sum of its low-pass (L) and high-pass (H) components. Now, define unsharp masking by

$$\begin{aligned} F &= aI - L \\ &= (a-1)I + I - L \\ &= (a-1)I + H \end{aligned} \tag{11}$$

which has a form similar to that in eqn.9. Hence, one of the many ways to interpret Laroche-Prescott's and Hamilton-Adams' algorithms, is an unsharp masking process. It may hence be expected that these processes will sharpen edges (only those in the cardinal directions, due to the manner in which they are implemented) in the resulting images as is observed in the results obtained from Laroche-Prescott's and Hamilton-Adams' interpolations (figs.9 to 18).

From Tables I and II, on the basis of simple majority, Freeman's algorithm outperforms the other algorithms. On the other hand, in two cases, it performs very poorly.

For Test Image_1, as can be seen from fig.9, Linear interpolation produces the *zipper* effect that had been mentioned earlier. This is because linear interpolation is a low pass filter process and hence incorrectly locates the edges in each color plane, introducing zipper [12]. Cok's interpolation reduces hue transitions over the edges since it interpolates the hue of the colors and not the colors themselves which reduces abrupt hue jumps producing fewer perceptual artifacts. Freeman's algorithm, using the median as an estimator, performs poorly because it first performs a linear interpolation for the green channel (a blur process), also introducing ripples. Laroche-Prescott's algorithm, using classifiers to interpolate in the preferred orientation reduces errors. Also, interpolating color differences (chrominance minus luminance), it utilizes information from two channels to precisely locate the edge. Hamilton-Adams' algorithm interpolates the luminance channel with a bias to the second derivative of the chrominance channel, locating the edge in the three color planes with better accuracy.

In Test Image_2, although we find the same trend in Linear and Cok interpolations as we did in Test Image_1, we find that Laroche-Prescott's and Hamilton-Adams' algorithms are able to reproduce the image exactly. This is attributed to the structure (and size) of their estimators and the width of the bars themselves (3 pixels).

In the Test Image_3, there are two factors that the algorithms are tested against, one is varying spatial frequencies and the other being non-cardinal edge orientations. Comparing figs.9 and 10 with fig.11, we observe that vertical and horizontal directions are reproduced with good clarity while edges along other orientations are not, alluding to the fact that almost all these algorithms (with the exception of Hamilton-Adams', which incorporates some diagonal edge information) are optimized for horizontal and vertical edge orientations. A similar observation is made for the CFA images.

Note that in Test Image_4, the edge between the two green patches has been estimated

with good accuracy by Laroche-Prescott's and Hamilton-Adams' algorithms. This is attributed to the fact that these two algorithms, unlike the others, use data from all the color planes for estimation. In this case, the data on either side of the edge being "similar", the estimate was correct.

Another trend observed is that Hamilton-Adams' algorithm performs better than Laroche-Prescott's algorithm. This is attributed to two reasons; one that the process of estimating the green channels in Hamilton-Adams' algorithm incorporates the second order gradient in the chrominance channels also, providing a better estimate while Laroche-Prescott's algorithm simply performs a prefential averaging. The second reason is that Hamilton-Adams' algorithm estimates diagonal edges while estimating the chrominance channels, giving it more sensitivity to non-cardinal chrominance gradients (which partially explains the slightly smaller error metrics for Test Image_3).

VI. Conclusion

It has been demonstrated that although the CFA pattern is very useful to capture multispectral data on a monolithic array, this system comes with associated problems of "missing samples". The estimation of these missing samples needs to be done in an efficient manner, at the same time, reproducing the original images with high fidelity.

In general, we observe two types of errors *zipper* effect errors (occur at intensity edges see fig.9 for this behavior) *confetti* errors (occur at bright pixels surrounded by a darker neighborhood see figs.14 and 13 for this behavior). Experimentally, it has been found that Freeman's algorithm is best suited for cases in which there is speckle behavior in the image, while Laroche-Prescott's and Hamilton-Adams' algorithms are best suited for images with sharp edges.

It is to be noted that demosaicking is not shift-invariant. Different results are observed

if the location of the edges is phase-shifted (the *zipper* effect errors show up either as blue-cyan errors or as orange-yellow errors depending upon edge-location, see fig.9). The result of demosaicking is hence a function of the edge location.

APPENDIX

Two of the color models suggested by the CIE which are perceptually balanced and uniform are the CIE-L*u*v* and the *CIE-L*a*b** color models. The *CIE-L*u*v** model is based on the work by MacAdams on the Just Noticeable Differences in color [16]. These color models are non-linear transformations of the XYZ color model. The transformation from the XYZ space to the *CIE-L*a*b** space is given by

$$L^* = \begin{cases} 116(\frac{Y}{Y_n})^{1/3} - 16) & \text{for} \quad \frac{Y}{Y_n} > 0.008856 \\ 903.3(\frac{Y}{Y_n}) & \text{otherwise} \end{cases}$$

$$a^* = 500\left[(\frac{X}{X_n})^{\frac{1}{3}} - (\frac{Y}{Y_n})^{\frac{1}{3}}\right]$$

$$b^* = 200\left[(\frac{Y}{Y_n})^{\frac{1}{3}} - (\frac{Z}{Z_n})^{\frac{1}{3}}\right]$$

where X_n, Y_n, Z_n are the values of X, Y, Z, for the appropriately chosen reference white; and where, if any of the ratios (X/X_n), (Y/Y_n) or (Z/Z_n) is less than or equal to 0.008856, it is replaced in the above formula by $7.787F + 16/116$ where F is (X/X_n), (Y/Y_n) or (Z/Z_n) as the case may be. The color differences in the *CIE-L*a*b** color space are given by $\Delta E^*_{ab} = \sqrt{(\Delta L^*)^2 + (\Delta a^*)^2 + (\Delta b^*)^2}$.

ACKNOWLEDGMENTS

We would like to thank the Army Research Office for its support in this work. This work is the first step in the development of a set of rugged, robust multispectral sensors for Army applications. We are also grateful to Pulnix America Inc. for providing us with a camera for this project.

REFERENCES

[1] B.E. Bayer, "Color imaging array," *United States Patent 3,971,065*, 1976.

[2] D.R. Cok, "Signal processing method and apparatus for producing interpolated chrominance values in a sampled color image signal," *United States Patent 4,642,678*, 1987.

[3] W.T. Freeman, "Median filter for reconstructing missing color samples," *United States Patent 4,724,395*, 1988.

[4] C.A. Laroche and M.A. Prescott, "Apparatus and method for adaptively interpolating a full color image utilizing chrominance gradients," *United States Patent 5,373,322*, 1994.

[5] J.F. Hamilton and J.E. Adams, "Adaptive color plan interpolation in single sensor color electronic camera," *United States Patent 5,629,734*, 1997.

[6] R. Kimmel, "Demosaicking: image reconstruction from color ccd samples," *IEEE Trans. Image Processing*, vol. 7, no. 3, 1999.

[7] H.J. Trussell, "Mathematics for demosaicking," *to be published IEEE Trans. Image Processing*, 2001.

[8] R. Ramanath, "Interpolation methods for the bayer color array," M.S. thesis, North Carolina State University, Raleigh, NC 27695, 2000.

[9] P. L. Vora, J. E. Farrell, J. D. Teitz, and D. H. Brainard, "Digital color cameras -1 - response models," *Hewlett-Packard Laboratory Technical Report*, , no. HPL-97-53, 1997.

[10] G. Bilbro and W. E. Snyder, "Optimization by mean field annealing," *Advances in Neural Information Processing Systems*, 1989.

[11] J.G. Proakis and D.G. Manolakis, *Digitla Signal Processing - Principles, Algorithms and Applications*, Prentice Hall Inc., New Jersey, third edition, 1998.

[12] J.E. Adams, "Interactions between color plane interpolation and other image processing functions in electronic photography," *Proc. SPIE Cameras and Systems for Electronic*

Photography and Scientific Imaging, vol. 2416, 1995.

[13] K. Topfer, J.E. Adams, and B.W. Keelan, "Modulation transfer functions and aliasing patterns of cfa interpolation algorithms," *IS&T PICS Conference*, 1998.

[14] J.E. Adams, "Design of practical color filter array interpolation algorithms for digital cameras," *Proc. SPIE, Real Time Imaging II*, vol. 3028, 1997.

[15] WD4 of ISO 17321, "Graphic technology and photography - color characterization of digital still cameras using color targets and spectral illumination," 1999.

[16] G. Wyszecki and W.S. Stiles, *Color Science – Concepts and Methods, Quantative Data and Formulae*, John Wiley and Sons, Inc., New York, second edition, 1982.

[17] M. L. Mahy, V. Eyckdenm, and A. Oosterlinck, "Evaluation of uniform color spaces developed after the adoption of cielab and cieluv," *Color Res. and Appl.*, vol. 19, no. 2, 1994.

[18] R.C. Gonzalez and R.E. Woods, *Digital Image Processing*, Addison Wesley, Reading, MA, 1992.

Project Title Assessment of monolithic imaging for missiles and smart ordnance

- **Dr. G.L.Bilbro, P.I.**
  - Dr. W. E. Snyder
  - Mr. R. Ramanath
- **Institution** North Carolina State University
- **Dates** 9/00-2/01
- **Funding** $20,000

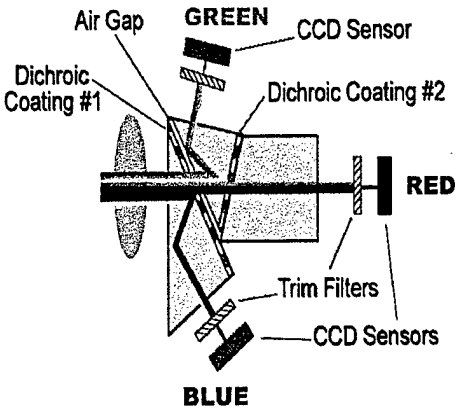

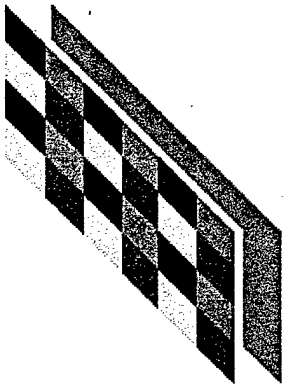

ATR for missile guidance

- **Problem** Large-range is needed to extend close-range Automatic Target Recognition
- **Potential solution** Multispectral imaging of unresolved targets (R. F. Sims, AMCOM)
- **Challenge** Sensors are large, expensive, and fragile
- **Proposal** Adapt *Bayer color array* from COTS color cameras to infrared image sensors

Technologies exist separately

- Semiconductor electronics
  - Next generation of Monolithic Infrared Detector Arrays, *NASA Goddard Space Flight Center* and *Discovery Semiconductors, Inc.*, A. M Joshi, M. Jhavbala, P. Shu
- Infrared filter materials
  - Broadening IR Applications through using spectral filters, *Inframetrics, Inc.,* A. C. Teich, R. Madding
- Red-Green-Blue Monolithic filters
  - Color imaging array, *United States Patent,* B. E. Bayer

Accomplishments

- MS degree awarded to R. Ramanath, "Interpolation methods for Bayer color array", 8/00
- Journal paper submitted: "Demosaicking methods for Bayer color arrays", JEI, 6/01
- Conference paper presented: "Robust Multi-Spectral Imaging Sensors for Autonomous Robots", OPTO South East, SPIE, Charlotte, NC, 10/00
- Follow-on DoD proposal submitted, G. Bilbro, 1/01
- Invention disclosed, "Seven band hexagonal image sensor", W. E. Snyder, NCSU, 11/00

This page is a copy of the title page of Mr. R. Ramanath's Master's Thesis. Mr. Ramanath's research was supported, in part, by the project reported herein, DAAD19-00-1-0498; all publications resulting from this research will properly cite the ARO project number. The thesis itself is available from NC State University, Raleigh, NC.

Interpolation Methods for the Bayer Color Array

by

Rajeev Ramanath

Master's Thesis submitted to the Faculty of the North Carolina State University in partial fulfillment of the requirements for the degree of

MS

in

Electrical Engineering

Approved

Dr. Wesley E. Snyder, Chair
Dr. Griff L. Bilbro, Member
Dr. Richard T. Kuehn, Member
Dr. Paul F. Hemler, Member

August 14, 2000
Raleigh, North Carolina

Abstract

RAMANATH, RAJEEV. Interpolation Methods for the Bayer Color Array (under the guidance of Dr. Wesley E. Snyder) Digital still color cameras working on single CCD-based systems have a mosaicked mask of color filters on the sensors. The Bayer array configuration for the filters is popularly used. This requires that the data be interpolated to recover all the scene information. Many existing interpolation (demosaicking) algorithms that can reconstruct the scene use modifications of the bilinear interpolation method, intro-ducing a variety of artifacts in the images. These algorithms have been investi-gated. A new method for restoring these color images using an optimization method known as Mean Field Annealing is introduced using a variety of image prior models. Their performance relative to existing demosaicking methods is included.